Wave-to-wire modelling of a vibro-impact wave energy converter for ocean data buoys

Shuai Chen * **Bingyong Guo** * **Hafiz A. Said** ** **Kunde Yang** *
John V. Ringwood **

* *School of Marine Science and Technology, Northwestern Polytechnical University, Xi'an 710072, China (e-mail: chen2023@mail.nwpu.edu.cn, b.guo@nwpu.edu.cn, ykdzym@nwpu.edu.cn)*
** *Centre for Ocean Energy Research, Department of Electronic Engineering, Maynooth University, Maynooth, Ireland, W23 X021 (e-mail: hafiz.said.2020@mumail.ie, John.Ringwood@mu.ie)*

Abstract: In this study, a wave-to-wire (W2W) model of a vibro-impact wave energy converter (VIWEC) is proposed for powering ocean data buoys. A battery and a supercapacitor are integrated to the VIWEC to form a hybrid energy storage system (HESS), in order to provide continuous and long-term DC power for the payloads of ocean data buoys. Based on the W2W model, controllers for maximising wave energy capture and managing the HESS are integrated, and then implemented by fully controllable AC/DC and DC/DC converters. On the basis of irregular waves, preliminary results show that the proposed W2W model with control can provide stable and continuous DC power. Thus, the proposed W2W model, integrated with HESS and control, can be used to investigate its feasibility and to assess its performance for ocean data buoys.

Keywords: Wave energy conversion, wave-to-wire modelling, hybrid energy-storage system, ocean data buoy, control of wave energy converter

1. INTRODUCTION

In general, the purpose of harvesting wave energy is to provide low-carbon electrical power for utility grids. However, the levelised cost of energy (LCoE) of wave energy, ranging from 120 to 470 dollars per MWh (Chozas, 2015), is higher than that of other renewable resources, e.g. wind or/and solar energy, since the wave energy technology is relatively immature. This makes wave energy uncompetitive or unviable in the utility market. On the other hand, many countries have made national strategies to accelerate the 'blue economy', and the demands of economical and clean *in-situ* power supplies in the niche market of ocean-based applications are emerging (IEA, 2020).

Ocean data buoys are broadly used all over the world for ocean observation and weather forecasting. For global ocean observation systems alone, there are about 4000 profiling floats, 1500 drifting buoys, and 400 moored buoys. Most ocean data buoys are equipped with batteries as a power supply, and some can be recharged by integrated solar panels, or wind turbines. Compared to offshore solar and wind energy, wave energy is of higher energy density and spatio-temporal availability, which makes it more applicable for powering ocean data buoys (Guo and Ringwood, 2021).

The current power consumption of ocean data buoys ranges from milliwatts, for profiling floats, to hundreds of watts, for large marine buoys (Green et al., 2019). Most ocean data buoys require power less than 100 W. However, end users are asking for longer deployments, higher sampling rates, more sensors, more options, improved communications, onboard data processing, underwater recharge, etc (Green et al., 2019). Thus, the potential power requirements may reach the order of kilowatts. Compared to the utility market, the rated capacities of wave energy converters (WECs) for ocean data buoys are much smaller, and the energy demands for ocean navigation and observation, coastal protection, desalination, multi-function offshore platforms, etc, can be satisfied by wave energy technologies. For those applications, conventional energy sources can be prohibitively expensive, mainly due to their offshore and remote deployment.

A number of WECs have been investigated for powering ocean data buoys. For instance, a high-latitude coastal weather buoy from National Data Buoy Center (NDBC) only requires an average power of 5 W, and a small WEC with a diameter of 1 m can produce an average power of 254 W, which is well beyond current and future power requirements of data buoys (Cavagnaro et al., 2020). For the NDBC buoy with a self-contained ocean observation payload, the average power consumption is around 5 W, and a small WEC with a horizontal pendulum of 20 kg can ensure a power output 5 W throughout the whole year, for the wave climate in the U.S. Pacific Northwest (Dizon et al., 2021). Another study on two oscillating
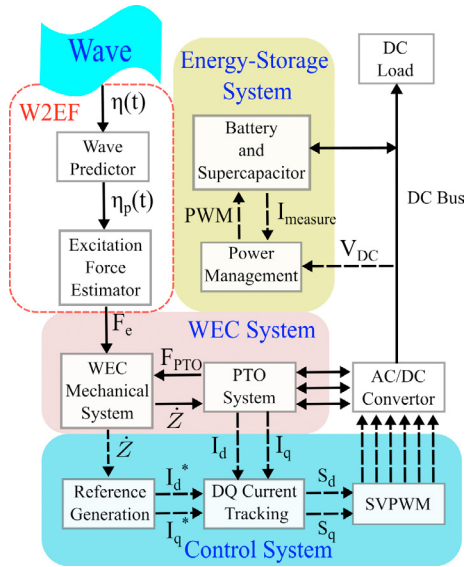
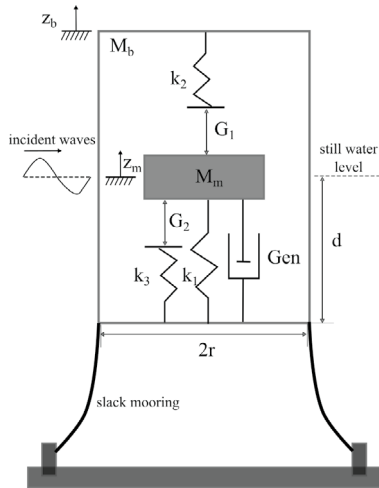Fig. 1. Schematic of the proposed wave-to-wire model.

Fig. 2. Schematic of the VIWEC.

water column type WECs by Henriques et al. (2016) also confirms the large potential and attractiveness of WECs in powering ocean data buoys for long-term deployment. In addition, a comparative study on modelling methods of a two-body heaving point absorber shows that linear frequency-domain modelling method is adequate for capturing WEC dynamics (Hamilton et al., 2021).

Some demonstrative sea trials have also shown the practicability of WECs for ocean observatories. The OPT PB3 device, with an internal energy storage system, was tested near New Jersey for 5 months, and its daily generated average power was 414 W, showing its commercial readiness for offshore applications, e.g. ocean observing, offshore oil and gas monitoring, communications and defence (Parsa et al., 2017). The OPT PB3 device was also tested in Chile for powering an integrated coastal ocean observatory for more than one year operation (Cortés et al., 2022). Another typical example is the Lifesaver WEC device, which continuously powered an adaptable monitoring package, rated at 600 W, for about 200 days (Cross and Rajagopalan, 2020). In addition, wave power can be directly used to drive vertical profilers (Osse et al., 2015; Rainville and

Pinkel, 2001). For further possibilities to power ocean data buoy, readers are referred to the review paper by McLeod and Ringwood (2022).

Few of the aforementioned studies give a detailed wave-to-wire (W2W) model of WECs for ocean data buoys, and this paper aims to establish a W2W model of a vibro-impact wave energy converter (VIWEC). As shown in Fig. 1, the W2W model includes a wave-to-excitation-force model, a VIWEC dynamical model, a power take-off (PTO) model, an energy storage model, and a control system. The mechanical structure of the VIWEC is shown in Fig. 2. The main body of the VIWEC is a semi-submersible cylindrical buoy with a self-contained inner mass, which is connected to the buoy by a supporting spring and a tubular permanent magnet linear generator (TPMLG). Inside the buoy, there are two impact springs attached to the buoy's ceiling and floor, working as a so-called vibro-impact mechanism (Guo and Ringwood, 2020). Numerical studies show that this impact mechanism can increase the power capture bandwidth in moderate sea states and improve survivability in extreme waves. As waves excite the VIWEC, the buoy and the inner mass oscillate, and their relative motion drives the TPMLG to produce electrical power. The power quality is expected to be poor, and a control system is integrated to maximise the captured wave power and to regulate the AC power into DC power, feeding the DC bus. A hybrid energy storage system (HESS), and a resistive DC load, are connected to the DC bus. With a proper power management strategy, the HESS can stabilise the voltage of the DC bus, even when the incoming wave is small and/or the DC load is varying. In this paper, numerical simulation, subjected to irregular waves, will be conducted to show the usefulness of the proposed W2W model of the VIWEC for control design, performance assessment, etc.

The reminder of this paper is organised as follows: Section 2 details the modelling of the VIWEC, while Section 3 discusses some control strategies used for wave power maximisation and HESS management. Section 4 briefly shows some numerical results with discussion, and some concluding remarks are drawn in Section 5.

2. WAVE-TO-WIRE MODELLING

This section describes the W2W modelling of the VIWEC with an integrated HESS for an ocean data buoy, including the dynamics of the buoy, the inner mass, the TPMLG and the HESS, given as follows.

2.1 Dynamics of the cylindrical buoy

Based on Cummins' equation, the dynamics of buoy are governed by

$$M_b \ddot{z}_b = f_{hs} + f_r + f_e + f_i + f_{pto}, \quad (1)$$

where M_b, $\ddot{z}_b$, f_{hs}, f_r, f_e, f_i and f_{pto} are the buoy mass, heave acceleration, hydrostatic force, radiation force, excitation force, buoy-mass interactive force and PTO force, respectively.

For a cylindrical heaving buoy, the hydrostatic force can be simply expressed as

$$f_{hs} = -\rho g \pi r^2 z_b, \quad (2)$$

where ρ, g and r represent the water density, gravitational acceleration and buoy radius, respectively.

The radiation force can be written as

$$f_r = -M_\infty \ddot{z}_b - k_r * \dot{z}_b, \qquad (3)$$

where M_∞ and $\dot{z}_b$ are the added mass at infinite frequency, and the buoy velocity in heave, respectively. k_r is the impulse response function (IRF) of the radiation force. In Eq. (3), the convolution term $f_{rc} = k_r * \dot{z}_b$ can be approximated by a state-space model with a finite order (Guo et al., 2017), given as

$$\dot{x}_r = A_r x_r + B_r \dot{z}_b, \qquad (4)$$
$$f_{rc} \approx C_r x_r, \qquad (5)$$

where $x_r \in \mathbb{R}^{n \times 1}$ is the state vector for the identified system, and $A_r \in \mathbb{R}^{n \times n}$, $B_r \in \mathbb{R}^{n \times 1}$, $C_r \in \mathbb{R}^{1 \times n}$ are the system matrices. n is the system order which is selected by trial and error using goodness of fit as a fidelity metric (Guo et al., 2017). In this study, $n = 5$ is used, and the goodness of fit is over 0.9982.

In the time domain, the excitation force is given as

$$f_e(t) = k_e(t) * \eta(t) = \int_{-\infty}^{\infty} k_e(t - \tau)\eta(\tau)d\tau, \qquad (6)$$

where $k_e(t)$ is the excitation IRF, which can be computed from its frequency response function (FRF). $k_e(t)$ is non-causal, and causalisation and approximation of the excitation were studied by Guo et al. (2018), in which a time-shifting technique was applied to causalise $k_e(t)$ to its causalised form $k_{e,c}(t)$, with causalisation time t_c ($t_c \geq 0$). Thus, the excitation force can be rewritten as

$$f_e(t) = k_e(t) * \eta(t) \qquad (7)$$
$$= k_e(t - t_c) * \eta(t + t_c) = k_{e,c}(t) * \eta_p(t), \qquad (8)$$

where $k_{e,c}(t) = k_e(t - t_c)$ and $\eta_p(t) = \eta(t + t_c)$ are the causalised excitation IRF and the predicted wave elevation advanced by t_c, respectively. In this paper, the predicted wave is assumed known, and readers interested in wave prediction are referred to Fusco and Ringwood (2010).

Similarly, Eq. (8) can be approximated by a finite order state-space model, written as

$$\dot{x}_e = A_e x_e + B_e \eta_p, \qquad (9)$$
$$f_e \approx C_e x_e + D_e \eta_p, \qquad (10)$$

where $x_e \in \mathbb{R}^{n \times 1}$ is the system state vector, and $A_e \in \mathbb{R}^{n \times n}$, $B_e \in \mathbb{R}^{n \times 1}$, $C_e \in \mathbb{R}^{1 \times n}$ and $D_e \in \mathbb{R}^{1 \times 1}$ are the system matrices, and n is the order. t_c and n are selected by trial and error using truncation error and goodness of fit as metrics (Guo et al., 2018). In this study, $t_c = 8$ s and $n = 13$ are used, and the identified excitation IRF is compared with its causualised counterpart, with a truncation error less than 0.0175 and a goodness of fit up to 0.9934.

2.2 Dynamics of the inner mass

The dynamics of the inner mass are governed by

$$M_m \ddot{z}_m = -f_{pto} - f_i, \qquad (11)$$

where M_m, z_m and $\ddot{z}_m$ represent the inner mass, and its displacement and acceleration in heave, respectively. The interaction force f_i depends on the relative displacement between the inner mass and the buoy, i.e. $z_r = z_m - z_b$. When the relative displacement is larger than, or equal to,

the upper gap G_1, i.e. $z_r \geq G_1$, the supporting spring (k_1) and the upper impact spring (k_2) are active. Therefore, f_i can be written as

$$f_i = k_1 z_r + k_2(z_r - G_1). \qquad (12)$$

When $G_1 > z_r > -G_2$, only the supporting spring (k_1) is active, and f_i can be written as

$$f_i = k_1 z_r. \qquad (13)$$

For the case $z_r \leq -G_2$, the supporting spring (k_1) and the lower impact spring (k_3) are active. Hence, f_i can be written as

$$f_i = k_1 z_r + k_3(z_r + G_2). \qquad (14)$$

2.3 Dynamics of the linear generator

The mathematical model of the TPMLG is the same as a conventional permanent magnet synchronous generator, given in the *dq-axis* as (Kundur and Malik, 2022)

$$U_d = R_s I_d + L_d \dot{I}_d - \omega_e I_q L_q, \qquad (15)$$
$$U_q = R_s I_q + L_q \dot{I}_q + \omega_e(I_d L_d + \phi_{pm}), \qquad (16)$$

where U_d, U_q, I_d, I_q are the voltages and currents for the *d-axis* and *q-axis*, respectively. ϕ_{pm} is the flux linkage constant, and ω_e is the electrical angular velocity. R_s, L_d and L_q are the synchronous resistance, *d-axis* inductance, and *q-axis* inductance, respectively. Therefore, the electrical angular velocity and PTO force are given as

$$\omega_e = \frac{\pi}{\tau_p} \dot{z}_r, \qquad (17)$$

$$f_{pto} = \frac{3\pi}{2\tau_p}[I_q(I_d L_d - \phi_{pm}) - I_d I_q L_q], \qquad (18)$$

where τ_p is pole pitch of the TPMLG, and $\dot{z}_r$ represents the relative velocity between the inner mass and the buoy.

2.4 Dynamics of the energy storage system

As shown in Fig. 1, the TPMLG is driven by the VIWEC, generating the corresponding force f_{pto} acting on the VIWEC. Meanwhile, the TPMLG produces three-phase AC power, which is regulated to DC power via an AC/DC converter, controlled by the switching signals (S_1, S_1', S_2, S_2', S_3, S_3'). On the DC bus side, a battery and supercapacitor are used to form the HESS, in order to stabilise the voltage of the DC bus and to power the DC load uninterruptedly.

In the study by Said and Ringwood (2021), the average modelling method is used to model the dynamics of the AC/DC converter and the buck-boost DC/DC converters, which shows advantages in control design and accelerated numerical simulation. However, some important features, e.g. ripples in current and voltage induced by the switching edges of the space vector pulse width modulation (SVPWM) and pulse width modulation (PWM) signals, are omitted. Therefore, this paper directly uses the MATLAB/SIMULINK models of the fully controllable universal AC/DC converter, buck-boost DC/DC converters, lithium-ion battery and supercapacitor, as shown in Fig. 3. These models are computationally expensive, especially when the frequencies of the SVPWM and PWM signals are high. On the other hand, these models show a high flexibility in investigating control implementation via power electronics with SVPWM and PWM signals.
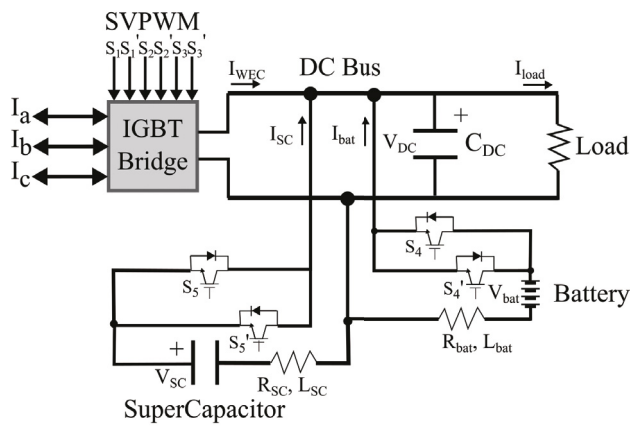
Fig. 3. Schematic of the hybrid energy-storage system.

3. CONTROL STRATEGIES

This section is devoted to the design and analysis of control strategies for the VIWEC and its HESS, in order to maximise wave power capture, using passive control, and to stabilise the DC voltage by switching the charge/discharge modes of the battery and supercapacitor.

3.1 Control of wave power capture

To maximise wave power capture, passive control with an optimal passive PTO damping coefficient R_{pto}, determined by an exhaustive search method, is applied. Thus, the PTO reference force f_{pto}^* is given as

$$f_{pto}^* = -R_{pto}\dot{z}_r. \tag{19}$$

For the TPMLG, f_{pto} is directly related to I_d and I_q. Therefore, the tracking of f_{pto}^* can be achieved by regulating I_d and I_q. The reference of the *d-axis* current is set to $I_d^* = 0$, which has two advantages: (i) to maximise the force-to-current ratio, and (ii) to attenuate the non-linearity of the non-linear term $\frac{3\pi}{2\tau_p}I_q I_d L_d$ in Eq. (18). Thus, the PTO force reference can be rewritten as

$$f_{pto}^* = -\frac{3\pi}{2\tau_p}\phi_{pm}I_q^*. \tag{20}$$

Combining Eqs. (19) and (20), the reference of the *q-axis* current is given as

$$I_q^* = -\frac{2\tau_p}{3\pi\phi_{pm}}R_{pto}\dot{z}_r. \tag{21}$$

Thus, passive control of the VIWEC becomes a tracking control problem for I_d and I_q.

The deviations of I_d and I_q from their references are given as

$$e_d = I_d^* - I_d, \tag{22}$$
$$e_q = I_q^* - I_q. \tag{23}$$

According to the Lyapunov theorem, in order to drive e_d and e_q to zero, their derivatives, $\dot{e}_d$ and $\dot{e}_q$, should meet

$$\dot{e}_d = -\lambda_1 e_d, \tag{24}$$
$$\dot{e}_q = -\lambda_2 e_q, \tag{25}$$

where λ_1 and λ_2, are positive real parameters. Combining Eqs. (15), (16), (22) and (23), $\dot{e}_d$ and $\dot{e}_q$ can be rewritten as
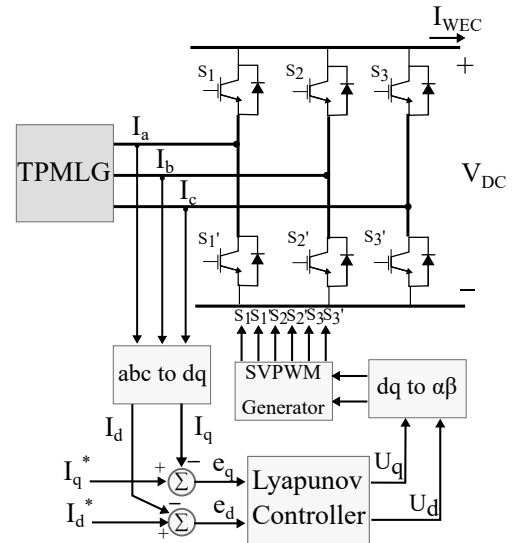

Fig. 4. Schematic of the control of the AC/DC converter.

$$\dot{e}_d = \dot{I}_d^* - \frac{1}{L_d}(U_d - R_s I_d + \omega_e L_q I_q), \tag{26}$$

$$\dot{e}_q = \dot{I}_q^* - \frac{1}{L_q}(U_q - R_s I_q - \omega_e(L_d I_d + \phi_{pm})), \tag{27}$$

where $\dot{I}_d^*$ and $\dot{I}_q^*$ represent the derivatives of *dq-axis* current references, respectively. Comparing Eqs. (22), (23), (26) and (27), with Eqs. (24)-(25), results in the control law for the AC/DC converter as

$$U_d = R_s I_d + \lambda_1 L_d e_d - \omega_e L_q I_q + L_d \dot{I}_d^*, \tag{28}$$
$$U_q = R_s I_q + \lambda_2 L_q e_q + \omega_e(L_d I_d + \phi_{pm}) + L_q \dot{I}_q^*. \tag{29}$$

As shown in Fig. 4, the Lyapunov-based controller is applied to achieve the tracking control problem for I_d and I_q, and implemented by generating SVPWM signals, i.e. S_1, S_1', S_2, S_2', S_3, S_3', to switch the AC/DC converter.

3.2 Control of energy-storage system

As shown in Fig. 5, the HESS control aims to stabilise the DC voltage, and to control the charge/discharge modes of the battery and the supercapacitor. To stabilise the DC voltage, a Lyapunov-based controller is used in the external control loop to achieve V_{DC} tracking, the tracking error between V_{DC} and its reference value V_{DC}^* is defined as

$$e_{DC} = V_{DC}^* - V_{DC}. \tag{30}$$

To drive e_{DC} to zero, its derivative $\dot{e}_{DC}$ should meet

$$\dot{e}_{DC} = -\lambda_3 e_{DC}, \tag{31}$$

where λ_3 is a positive real parameter. As shown in Fig. 3, the dynamics of V_{DC} are given as follows

$$C_{DC}\dot{V}_{DC} = I_{WEC} + I_{SC} + I_{bat} - I_{load}. \tag{32}$$

Combining Eqs. (30)-(32), the control law of HESS can be given as

$$I_{bat} + I_{SC} = C_{DC}\lambda_3 e_{DC} - I_{WEC} + I_{load} + \dot{V}_{DC}^*, \tag{33}$$

where $I_{bat} + I_{SC}$ represent the desired current value of battery and supercapacitor to the DC bus, and $\dot{V}_{DC}^*$ represents the derivative of V_{DC}^*.
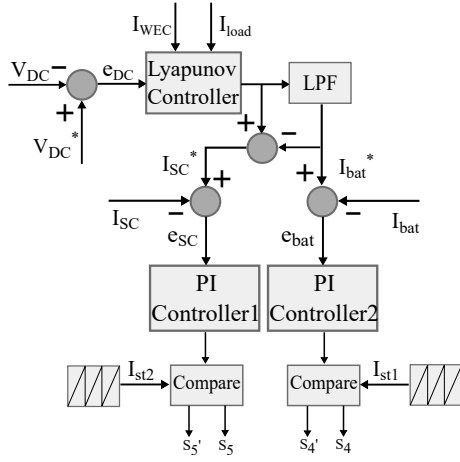
Fig. 5. Schematic of the HESS control.

As shown in Fig. 5, the output of the Lyapunov-based controller is used as the current reference signal for the HESS. A low-pass filter (LPF) is used to divide the HESS current reference signal into high-frequency and low-frequency parts. The former one is treated as the reference signal for the supercapacitor (I_{SC}^*), while the latter one is viewed as the reference signal for the battery (I_{bat}^*).

In the inner control loop, a PI controller is used to achieve tracking of I_{bat}, with the current error signal ($e_{bat} = I_{bat}^* - I_{bat}$) as input, and its output signal compared with a sawtooth signal (I_{st1}) to generate a PWM signal S_4 for switching the buck-boost DC/DC converter. The control of the supercapacitor is similar to that of the battery, and, hence, is not repeated here. In general, $S_i' = \neg S_i$ holds for $i = 1, 2, \cdots, 5$. The parameters of the controllers in Figs. 4 and 5 are determined in a trial and error manner. In addition, the frequency of the PWM signal for the HESS control in Fig. 5 can be different from that for AC/DC control in Fig. 4.

4. RESULTS AND DISCUSSION

The performance of the proposed W2W model with the HESS and control is evaluated by numerical simulation in the MATLAB/SIMULINK environment. The parameters for simulation are given in Table 1. The irregular waves are generated according to the JONSWAP spectrum with a peak enhancement factor of 3.3, and the sea states is represented by a significant wave height of $H_s = 0.85$ m and a peak period of $T_p = 5.7$ s. Correspondingly, the irregular waves are shown in Fig. 6.

The tracking performance of the PTO force, battery current, supercapacitor current and DC voltage is shown in Fig. 7. In Fig. 7(a), the PTO force follows its reference signal well, with some deviations at peaks and troughs. In Fig. 7(b)-(c), the battery and supercapacitor currents converge to their reference signals with good accuracy, which indicates that the strategy of separating low-frequency and high-frequency components of HESS current is effective. In Fig. 7(d), the DC bus voltage can track its reference well, and the tracking error is less than 1%.

Compared to the simulation results by Said and Ringwood (2021), the results in Fig. 7 have more obvious jitters, mainly due to the difference in modelling methods. The

Table 1. System parameters for simulation.

| VIWEC	
Cylinder radius r	1 m
Cylinder height h	2 m
Added mass at infinite frequency M_∞	1883 kg
Buoy mass M_b	1220 kg
Inner mass M_m	2000 kg
Support spring stiffness k_1	1×10^4 N/m
Impact spring stiffness k_2, k_3	3×10^5 N/m
Spring-mass gap distance G_1, G_2	0.7, 0.7 m
TPMLG	
Resistance R_s	2.9 Ω
Inductance L_d, L_q	0.022 H, 0.022 H
Flux linkage ϕ_{pm}	1.0023 Wb
Pole pitch τ_p	0.0288 m
Controller	
PTO damping coefficient R_{pto}	1600
Lyapunov-based controller $\lambda_1, \lambda_2, \lambda_3$	$1000, 50000, 500$
PI controller $k_{p1}, k_{i1}, k_{p2}, k_{i2}$	$1, 0.05, 1, 0.05$
Energy storage system	
Battery's voltage and capacity	48 V, 20 Ah
Supercapacitor's voltage and capacitance	64 V, 20 F
Inductance L_{bat}, L_{SC}	1 mH, 1 mH
LPF natural frequency and damping ratio	0.1 Hz, 1
DC capacitor C_{DC}	0.1 F
DC voltage reference V_{DC}^*	150 V
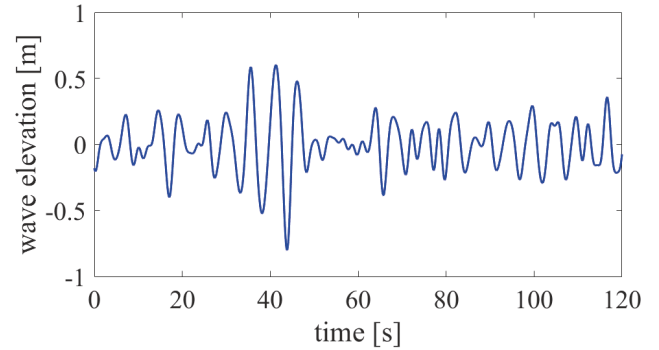
Fig. 6. Irregular waves for the sea state of $H_s = 0.85$ m and $T_p = 5.7$ s.

average modelling method is used by Said and Ringwood (2021) to smooth the dynamics power electronics and to accelerate numerical computation. However, SVPWM and PWM signals are directly used in this paper, and the results are significantly influenced by their frequencies. Thus, increasing the frequencies of SVPWM and PWM signals can improve the tracking performance. Consequently, computation cost will be higher. In this study, an Intel Core i5-12500H processor of the 12th generation @ 2.50 GHz is used, with a memory (RAM) of 16.0 GB. For the results in Fig. 7, the simulation time span is 120 s, with a sampling interval of 0.001 s, it takes 175.62 s to run a trial.

5. CONCLUSION

This paper derives a W2W model of the VIWEC with integrated HESS and control system to serve as an *in-situ* power supply for ocean data buoys. Wave power maximising control is implemented by a AC/DC converter with SVPWM signals, and the HESS control is realised by buck-boost DC/DC converters with PWM signals. Preliminary numerical results with irregular waves show that the W2W model can be used for control design and assessing the
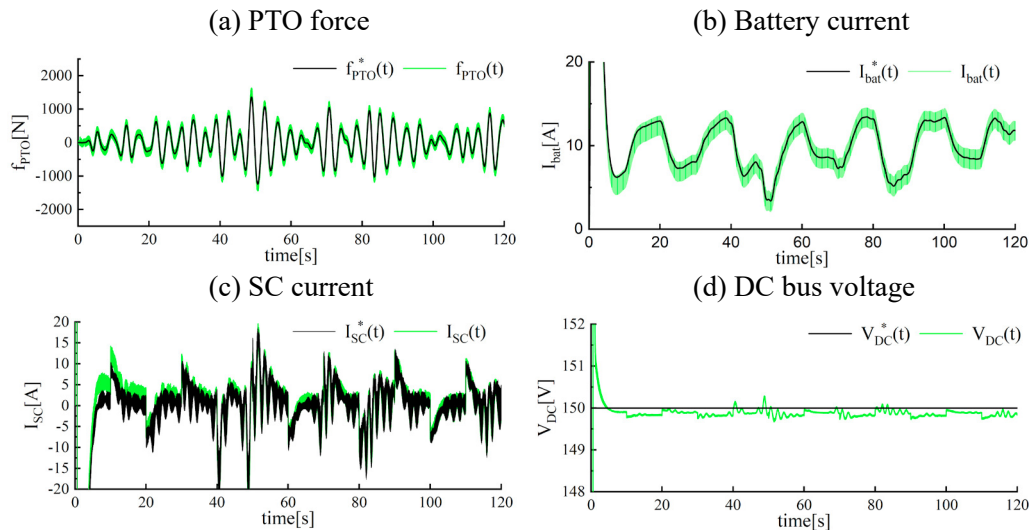
(a) PTO force

(b) Battery current

(c) SC current

(d) DC bus voltage

Fig. 7. Tracking performance of the PTO force, battery current, supercapacitor current and DC voltage in (a)-(d), respectively.

feasibility of the VIWEC for ocean data buoys, as passive control, Lyapunov-based and PI controllers can be easily replaced by other control strategies.

REFERENCES

Cavagnaro, R.J., Copping, A.E., Green, R., Greene, D., Jenne, S., Rose, D., and Overhus, D. (2020). Powering the blue economy: Progress exploring marine renewable energy integration with ocean observations. *Mar. Technol. Soc. J.*, 54(6), 114–125.

Chozas, J. (2015). International levelised cost of energy for ocean energy technologies. Technical report.

Cortés, J., Lucero, F., Suarez, L., Escauriaza, C., Navarrete, S.A., Tampier, G., Cifuentes, C., Cienfuegos, R., Manriquez, D., Parragué, B., et al. (2022). Open sea lab: An integrated coastal ocean observatory powered by wave energy. *J. Mar. Sci. Eng.*, 10(9), 1249.

Cross, P. and Rajagopalan, K. (2020). Wave energy converter deployments at the navy's wave energy test site: 2015-2019. *Mar. Technol. Soc. J.*, 54(6), 91–96.

Dizon, C., Cavagnaro, R.J., Robertson, B., and Brekken, T.K. (2021). Modular horizontal pendulum wave energy converter: Exploring feasibility to power ocean observation applications in the us pacific northwest. *IET Renew. Power Gener.*, 15(14), 3354–3367.

Fusco, F. and Ringwood, J.V. (2010). Short-term wave forecasting for real-time control of wave energy converters. *IEEE Trans. Sust. Energy*, 1(2), 99–106.

Green, R., Copping, A., Cavagnaro, R.J., Rose, D., Overhus, D., and Jenne, D. (2019). Enabling power at sea: Opportunities for expanded ocean observations through marine renewable energy integration. In *OCEANS 2019-MTS/IEEE Seattle*, 1–7. IEEE.

Guo, B., Patton, R., Jin, S., Gilbert, J., and Parsons, D. (2017). Nonlinear modeling and verification of a heaving point absorber for wave energy conversion. *IEEE Trans. Sustain. Energy*, 9(1), 453–461.

Guo, B., Patton, R.J., Jin, S., and Lan, J. (2018). Numerical and experimental studies of excitation force approximation for wave energy conversion. *Renew. Energy*, 125, 877–889.

Guo, B. and Ringwood, J. (2020). Non-linear modeling of a vibro-impact wave energy converter. *IEEE Trans. Sust. Energy*, 12(1), 492–500.

Guo, B. and Ringwood, J.V. (2021). A review of wave energy technology from a research and commercial perspective. *IET Renewable Power Generation*, 15(14), 3065–3090.

Hamilton, A., Cazenave, F., Forbush, D., Coe, R.G., and Bacelli, G. (2021). The mbari-wec: a power source for ocean sensing. *Journal of Ocean Engineering and Marine Energy*, 7(2), 189–200.

Henriques, J., Portillo, J.C., Gato, L., Gomes, R., Ferreira, D., and Falcão, A. (2016). Design of oscillating-water-column wave energy converters with an application to self-powered sensor buoys. *Energy*, 112, 852–867.

IEA (2020). Blue economy and its promising markets for ocean energy. Technical report.

Kundur, P.S. and Malik, O.P. (2022). *Power system stability and control*. McGraw-Hill Education.

McLeod, I. and Ringwood, J.V. (2022). Powering data buoys using wave energy: a review of possibilities. *Journal of Ocean Engineering and Marine Energy*, 8, 417–432.

Osse, T.J., Meinig, C., Stalin, S., and Milburn, H. (2015). The prawler, a vertical profiler powered by wave energy. In *OCEANS 2015-MTS/IEEE Washington*, 1–8. IEEE.

Parsa, K., Mekhiche, M., Sarokhan, J., and Stewart, D. (2017). Performance of opt's commercial pb3 power-buoy during 2016 ocean deployment and comparison to projected model results. In *International Conference on Offshore Mechanics and Arctic Engineering*, 1–7.

Rainville, L. and Pinkel, R. (2001). Wirewalker: An autonomous wave-powered vertical profiler. *J. Atmos. Ocean Technol.*, 18(6), 1048–1051.

Said, H.A. and Ringwood, J.V. (2021). Intelligent control of a dc microgrid consisting of wave energy converter (wec) and hybrid energy storage system (hess). In *European Wave and Tidal Energy Conference*, 1–9.